Application of material point methods for cutting process simulations

Ravindra Ambati [a], Xiaofei Pan [a], Huang Yuan [a,*], Xiong Zhang [b]

[a] Department of Mechanical Engineering, University of Wuppertal, Gaußstr. 20, Wuppertal, Germany
[b] School of Aerospace, Tsinghua University, Beijing 100084, PR China

ARTICLE INFO

ABSTRACT

The finite element method (FEM) is popular in cutting process simulations. Due to large strains and element distortions the FEM simulations are confronted with numerical difficulties. In the present contribution the material point method (MPM) is developed for cutting process simulations. Due to special working condition in cutting, a special contact algorithm has been applied for the simulation. Verification of computations confirm that the MPM generates realistic chip morphologies. The plastic strain and temperature distributions are compared with the FEM computations. It is found that the MPM provides a smoother chip formation and less strain localizations. The predictions on friction effect and feed influence agree with experimental observations. The investigation shows that the material point method is an efficient alternative method to the finite element methods.

1. Introduction

Machining process is one of the prominent industrial applications in the manufacturing field. It is necessary to make advancements in the manufacturing industry with the application of present technology. The best of it is to use the numerical methods to analyze machining processes. Application of numerical methods has brought enormous changes in the engineering field. The fundamental process in manufacturing industrial applications is cutting. The simplest form of analyzing cutting process is to consider the orthogonal cutting. Many works have been performed to analyze cutting process analytically, numerically and experimentally. The mechanics incurred in cutting process has been explained by Merchant in the year 1945 by considering plastic behavior of material [1,2]. This is the initial motivated work for progressive research in metal cutting. In early 1970s numerical field has shown its significance in wide range of fields. During 1980s numerical works on cutting process have been carried out. In 1985 Strenkowski and Carroll started publishing numerical work on cutting [3,4]. In 1989 Howerton presented experimental work comparing with numerical simulations [5]. Bäker has explained some of the computational issues regarding energy dissipation in chip formation and thermal effects on chip morphology [25,26]. Aurich has presented brief discussion about the orthogonal metal cutting using finite element method [6]. In later years researchers identified element deformation as the fundamental problem for numerical modeling of cutting process. The severe deformation of material during cutting process leads to heavy distortion in finite elements in numerical modeling of cutting and diminishes accuracy of the results. Hence it is important to develop methods to reduce the element deformation. Partially the element distortion has been overcome with the application of techniques like remeshing, adaptive meshing and ALE. Remeshing technique has been applied to reduce the element distortion. But the remeshing technique has its own limitations like reformation of the mesh due to which previous time step stress field will be neglected, hence error will occur in the computation of field variables. Later adaptive meshing and Arbitrary Lagrangian Eulerian (ALE) methods have been applied for cutting process to reduce element distortion effects [9–11]. Even though these techniques partially solve the element distortion problem, there are other round off errors. In [7] the element size in using FEM is explained. The numerical results are sensitive to the FE mesh used [8]. Hence it is necessary to develop or apply new method to reduce the element distortion effect without significant errors. This leads to apply the element free techniques for high deformation processes (machining processes) to remove the element distortion problem.

The first element free technique applied to cutting process is SPH (Smoothed Particle Hydrodynamics). In 1997 Heinstein and Segalman first applied SPH method for orthogonal cutting process simulations [12]. The authors mainly explained the application and advantages of the method, certainly element deformation handling at the vicinity of cutting tool edge. In later years very few works have been published on cutting with SPH. In 2007 Limido et al. did significant work on cutting process with the application of

SPH [13], mainly explained the reliability of the SPH method by comparing with FEM numerical approach and experimental data. There are other meshless techniques, but the active portion of the work on cutting is done only with SPH. The published works on cutting with meshless techniques are very few when compare to FEM, this might be due to complexities incurred in developing the method. For successful modeling of high deformation processes element free methods are generally more convenient. Hence in present contribution MPM (material point method) has been developed for cutting process simulations.

The MPM is evolved from PIC (particle in cell) method and is a finite element based particle method [14]. Chen and Schreyer started developing MPM from PIC [16] in 1994, which is the initial development of MPM. Later Sulsky contributed many works on MPM, his method is further extended by Bardenhagen et al. to include frictional contact [17,19]. Recently many works have been published with the MPM for transient dynamic problems [21,23]. The results confirm that the MPM is an alternative method to FEM in high deformation dynamic problems as there is no need of re-meshing or adaptive meshing with MPM [24]. But the density of material points used in the computation will influence the simulations results.

MPM is a more expensive method compare to FEM, because MPM stores data in material points as well in back ground mesh. Oscillations in the results with MPM is taken care by using the generalized interpolation material point technique (GIMP) [21,23]. Strain localization in MPM is very sensitive to material points. The simulation work using GIMP is presented in [22]. As MPM does not contain any mesh, there is no question arises on the lines of element distortion. The external visualization of MPM is similar to meshless method, though the computational approach is different, this advantages over FEM. In the present work the MPM is applied for simulation of cutting process based on the visco-plastic models.

2. Computational approaches

In this section the material point method (MPM) and generalized interpolation material point method (GIMPM) will be reviewed. The main difference between the two methods is the order of shape functions. In MPM C_0 order shape functions and in GIMPM C_1 order shape functions are used.

2.1. Material point method (MPM)

Although there are several kinds of meshless methods developed in last decades, their methodological complexities and computational limitations give scopes for other methods to apply for certain processes. For this reason MPM is developed as one of the spatial discretization methods. The essential idea behind this method development is to use it for fluid and solid mechanics problems. Though the MPM method is not utilized concepts of fully developed meshless method, it incurs Lagrange and Eulerian concepts to solve the problem. Hence it can be used successfully for high deformation rate processes, as explosive simulations, high speed machining process, etc. MPM is particle method, developed based on PIC (particle in cell) method. Initially the method is developed for fluid applications, later has been applied for large deformation and large rotation problems successfully. For continuum bodies, the mass conservation equation is

$$\frac{\mathrm{d}\rho}{\mathrm{d}t} + \rho \nabla \cdot \mathbf{v} = 0 \tag{1}$$

and conservation equation for momentum is given by

$$\rho \frac{\mathrm{d}\mathbf{v}}{\mathrm{d}t} = \nabla \cdot \boldsymbol{\sigma} + \rho \mathbf{b}, \tag{2}$$

where ρ is the mass density, $\mathbf{v}$ is the velocity vector, $\boldsymbol{\sigma}$ is stress tensor and $\mathbf{b}$ is the body force vector. In MPM, the continuum body is discretized with N_p material particles. Each material particle carries the information of position, velocity, mass, density, stress, strain and all other internal state variables necessary for the constitutive model. Since the mass of each particle is fixed, Eq. (1) is automatically satisfied. At each time step, the mass and velocities of the material particles are mapped onto the background computational mesh (cell). The mapped velocity $\mathbf{v}_j$ of the node j is obtained through the following equation:

$$\sum_j m_{ij}\mathbf{v}_j = \sum_p m_p \mathbf{v}_p N_i(\mathbf{x}_p), \tag{3}$$

where m_p, $\mathbf{v}_p$ and $\mathbf{x}_p$ are the mass, velocity and position of the particle p, respectively. N_i is the shape function of the background cell. For 3D problem, a eight nodal cell is employed with the shape functions given by

$$N_i = \frac{1}{8}(1 + \xi\xi_i)(1 + \eta\eta_i)(1 + \zeta\zeta_i), \tag{4}$$

where ξ, η and ζ are the natural coordinates of the material particle in the cell along the x, y and z directions. The shape functions are the same as in the finite element method.

In Eq. (3) the consistent mass matrix, m_{ij}, is given by

$$m_{ij} = \sum_p m_p N_i(\mathbf{x}_p) N_j(\mathbf{x}_p). \tag{5}$$

In practice, we generally replace m_{ij} with a lumped diagonal mass matrix, $m_i \delta_{ij}$ (no summation over i), so that Eq. (3) becomes

$$m_i \mathbf{v}_i = \sum_p m_p \mathbf{v}_p N_i(\mathbf{x}_p), \tag{6}$$

where lumped mass is represented by

$$m_i = \sum_p m_p N_i(\mathbf{x}_p). \tag{7}$$

After the information mapped from material points to mesh nodes, the discrete formulation of Eq. (2) on the mesh nodes can be obtained. The weak form of Eq. (2) is formulated based on the standard procedure as in the finite element method,

$$\int_\Omega \frac{\rho \delta \mathbf{v} \cdot \mathrm{d}\mathbf{v}}{\mathrm{d}t} \mathrm{d}\Omega + \int_\Omega \delta(\mathbf{v}\nabla) \cdot \boldsymbol{\sigma} \mathrm{d}\Omega - \int_{\Gamma_t} \delta\mathbf{v} \cdot \mathbf{t}\mathrm{d}\gamma - \int_\Omega \rho\delta\mathbf{v} \cdot \mathbf{b}\mathrm{d}\Omega$$
$$= 0, \tag{8}$$

where Ω is the current configuration of the continuum, Γ_t is the traction boundary, $\boldsymbol{\sigma}$ is the stress tensor, $\mathbf{t}$ is the external force vector and $\mathbf{b}$ is the body force vector. Since the continuum bodies are described with a finite set of material particles, the mass density can be written as,

$$\rho(\mathbf{x}) = \sum_p^{N_p} m_p \delta(\mathbf{x} - \mathbf{x}_p), \tag{9}$$

where δ is the Dirac delta function with dimension of the inverse of volume. From above equations it is deduced that

$$m_i \frac{\mathrm{d}\mathbf{v}_i}{\mathrm{d}t} = (\mathbf{f}_i)^{int} + (\mathbf{f}_i)^{ext}. \tag{10}$$

Above m_i is lumped mass, $(\mathbf{f}_i)^{int}$ and $(\mathbf{f}_i)^{ext}$ are the internal force and external force vectors which read separately

$$(\mathbf{f}_i)^{int} = -\sum_{p=1}^{N_p} m_p \boldsymbol{\sigma} \cdot (\triangle N_i)/\rho_p, \tag{11}$$

$$(\mathbf{f}_i)^{ext} = -\sum_{p=1}^{N_p} N_i \mathbf{b}_p + \mathbf{f}_i^c, \tag{12}$$

where the vector $\mathbf{f}_i^c$ is the contact force which is the external nodal force not including the body force. In the MPM formulated above C^0 order shape functions are used, which makes the significant difference from the GIMP (generalized interpolation material point) method. The weak form of momentum equation is solved on background mesh at each time step and the computed acceleration is used to update the particles data. Later the updated particle data is used to reinstate the position and coordinates of the background mesh nodes. Hence at each time step the momentum equation is solved on the background mesh.

2.2. Generalized interpolation material point method

In the early version of MPM, the cell shape function N_i is not smoothed in the construction of the weighting function which causes the numerical noise as the material points cross computational mesh boundaries. Everything is similar between MPM and GIMPM except the order of shape functions. The order of shape functions in MPM is C_0, whereas the order of shape functions in GIMP is C_1. For GIMP the following smoothed shape functions are used [18],

$$N_i = \Phi(r_x)\Phi(r_y), \tag{13}$$

where $r_x = |x_p - x_i|/L$ and $r_y = |y_p - y_i|/L$, L is the length of the cell and $\Phi(r)$ is given as follows

$$\Phi(r) = \begin{cases} \frac{7-16r^2}{8}, & r \leqslant 0.25 \\ 1-r, & 0.25 < r \leqslant 0.75 \\ \frac{(5-4r)^2}{16}, & 0.75 < r \leqslant 1.25 \\ 0, & r > 1.25. \end{cases} \tag{14}$$

The formulations of the weak form equation as well as force vector assignments are similar to that of conventional MPM method. The algorithm for MPM computations is summarized as follows:

1. With the given particle data like mass, m_p, position, $\mathbf{x}_p$, velocity, $\mathbf{v}_p$, mass density, ρ_p, and stress $\boldsymbol{\sigma}$ the lumped mass matrix can be calculated from Eq. (7) and solve for the nodal velocity from Eq. (6) and form the internal force Eq. (11).
2. Solve the momentum equation for the nodal accelerations and velocities in a Lagrangian frame from the following equation:

$$m_i[\mathbf{v}_i^{n+1} - \mathbf{v}_i^n] = \Delta t \mathbf{f}_i^{int}. \tag{15}$$

3. Update the field variables at material points by mapping the computed nodal values using the element shape functions (C_0 and C_1 order shape functions for MPM and GIMP, respectively). Positions and velocities of particle are updates as following:

$$\mathbf{x}_p^{n+1} = \mathbf{x}_p^n + \Delta t \sum_i \mathbf{v}_i^{n+1} N_i(\mathbf{x}_p^n) \tag{16}$$

and

$$\mathbf{v}_p^{n+1} = \mathbf{v}_p^n + \sum_i \left[\mathbf{v}_i^{n+1} - \mathbf{v}_i^n\right] N_i\left(\mathbf{x}_p^n\right). \tag{17}$$

Along with updating the deformation gradient for each particle, compute the strain using computed deformation gradient and solve constitutive equation to update the stress $\boldsymbol{\sigma}$.

4. Repeat the above procedure for further time steps.

MPM has its own advantages and disadvantages. All the important necessary data is carried out by particles, the background cell is only used to get data from material points after each time step, at the end of each time step the mesh comes into original state from deformed state. Particles keep carrying the computed data from step to step. Hence it is more applicable to large deformation processes. The method has similar advantages as ALE (Arbitrary Lagrange Eulerian) method but without mesh, hence can be used for all ALE applications rather with precise computations and without typical problems related to large deformations.

However, MPM is more expensive in terms of storage than other methods, because it need to store the data from material points as well from background cell. The boundaries should be treated precisely. If the particles cross the boundary of background cell, severe numerical errors occurs. Furthermore, the accuracy of integration and resolution of the solution is lower than the FEM.

2.3. Contact algorithm in MPM

The contact phenomenon has significant impact on the simulation results in MPM. Hence better understanding of contact algorithm is important to simulate processes using MPM. The initial detailed contact algorithm has been given by Bardenhagen et al [20]. According to Bardenhagen [17] the contact algorithm is intended to solve motion and deformation of the bodies. The bodies are moving in single valued velocity field $\mathbf{v}_i$ applied to nodes $i = 1, \ldots, N_n$. As this velocity is computed with Eq. 6, it is been called as center-of-mass velocity field. $\mathbf{v}_i^b$ represents the velocity of a node related to particular body, where b ranges over a number of bodies and i ranges over the nodes $i = 1, \ldots, N_n$. Where N_n represents the number of nodes. Since the shape functions have compact support, only those nodes in the vicinity of the body will have a meaningful velocity and the velocity at all other nodes will be zero. If one body is isolated with others, not in contact with others, then the two velocity fields $\mathbf{v}_i^b$ and $\mathbf{v}_i$ will be same in the neighborhood of that body. When the two bodies approach each other, then these two velocity fields differ. Thus it can be concluded that both bodies are nearing each other to come in contact. The constraint to define the contact between two bodies is defined as following:

$$(\mathbf{v}_i^b - \mathbf{v}_i) \cdot \mathbf{n}_i^b > 0. \tag{18}$$

In the equation above $\mathbf{n}_i^b$ denotes the normal vector of body b at node i. This is the simple condition to define the contact between two bodies. With consider friction the contact algorithm is more complicated. Sliding and sticking force will come into playing [17]. The main drawback of Bardenhagen contact algorithm is that, the premature contact occurs because the velocities of different bodies are mapped on the same nodes although the distance between the bodies may be still two or more times of the length of the cell. Hence the distance between two bodies is used as the main criterion to define contact [22]. GIMPM with contact algorithm based on distance between two bodies has been applied for present simulations. In new contact algorithm if the velocities of bodies A and B are mapped on the same node i (Fig. 1), then the distance between bodies A and B is calculated. The distance between bodies A and B is represented by D_i^{AB}, which can be calculated as

$$D_i^{AB} = \mathbf{n}^{AB} \cdot \mathbf{d}_i^A - \mathbf{n}^{AB} \cdot \mathbf{d}_i^B, \tag{19}$$

where $\mathbf{n}^{AB}$ is normal direction of contacting interface pointing from bodies A to B. $\mathbf{d}_i^A$ and $\mathbf{d}_i^B$ are the vectors pointing to node i from bodies A and B, respectively. $\mathbf{n}^{AB} \cdot \mathbf{d}_i^A$ and $\mathbf{n}^{AB} \cdot \mathbf{d}_i^B$ can be determined as follows:

$$\mathbf{n}^{AB} \cdot \mathbf{d}_i^A = \max\left(\mathbf{d}_i^{A^m} \cdot \mathbf{n}^{AB}\right), \tag{20}$$

here $m = 1, 2, \ldots, N_A$ and particle A^m belongs to body A.

$$\mathbf{n}^{AB} \cdot \mathbf{d}_i^B = \max\left(\mathbf{d}_i^{B^m} \cdot \mathbf{n}^{AB}\right), \tag{21}$$
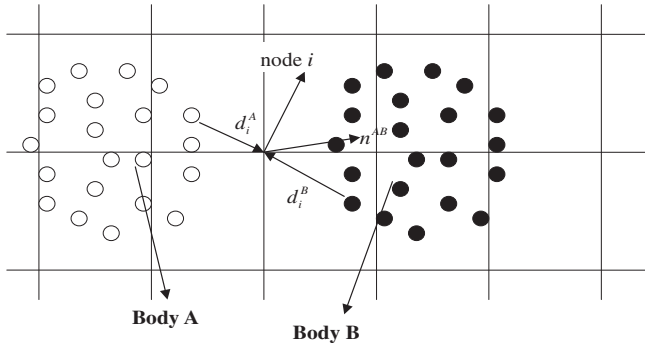
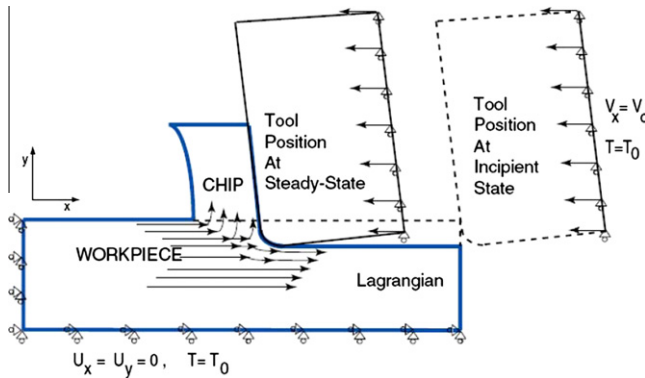**Fig. 1.** Representation of distance between bodies and normal vector.

Fig. 2. Sketch of the computational cutting model [30].

Table 1
Properties of the material of AISI 4340.

Density, ρ (g/mm^3)	0.00783
Elastic modulus, E (MPa)	2.07e + 5
Poisson's ratio, v	0.3
Specific heat, C_p (mJ g^{-1} °C^{-1})	480
Thermal conductivity, k (W mm^{-1} °C^{-1})	0.044
Expansion (mm mm^{-1} °C^{-1})	1.35e−5
T_{Melt} (°C)	1300
T_{Room} (°C)	25

here $m = 1, 2, \ldots, N_B$ and particle B^m belongs body B. N_A and N_B are the number of material points belongs to body A and B and $d_i^{A^m}$ and $d_i^{B^m}$ are the vectors pointing to node i from particles A_m and B_m, respectively.

The constraint for contact with the distance between bodies based theorem can be defined as

$$D_i^{AB} \leqslant L/2, \tag{22}$$

here L is the length of the defined cell. If Eq. (22) is satisfied, the velocities of body A and B are adjusted to new values. Hence all field variables are updated. During the course of contact the accelerations of bodies A and B are equal.

$$\mathbf{a}_i^A \cdot \mathbf{n}_i^{AB} = \mathbf{a}_i^B \cdot \mathbf{n}_i^{AB}. \tag{23}$$

From the Newton's second law, normal contact force ($\mathbf{f}_i^{nor}$) and accelerations of body A and B ($\mathbf{a}_i^A$ and $\mathbf{a}_i^B$) are calculated. The normal contact force must be non-negative for active contact. When the normal contact force is negative the bodies will be no more in contact.
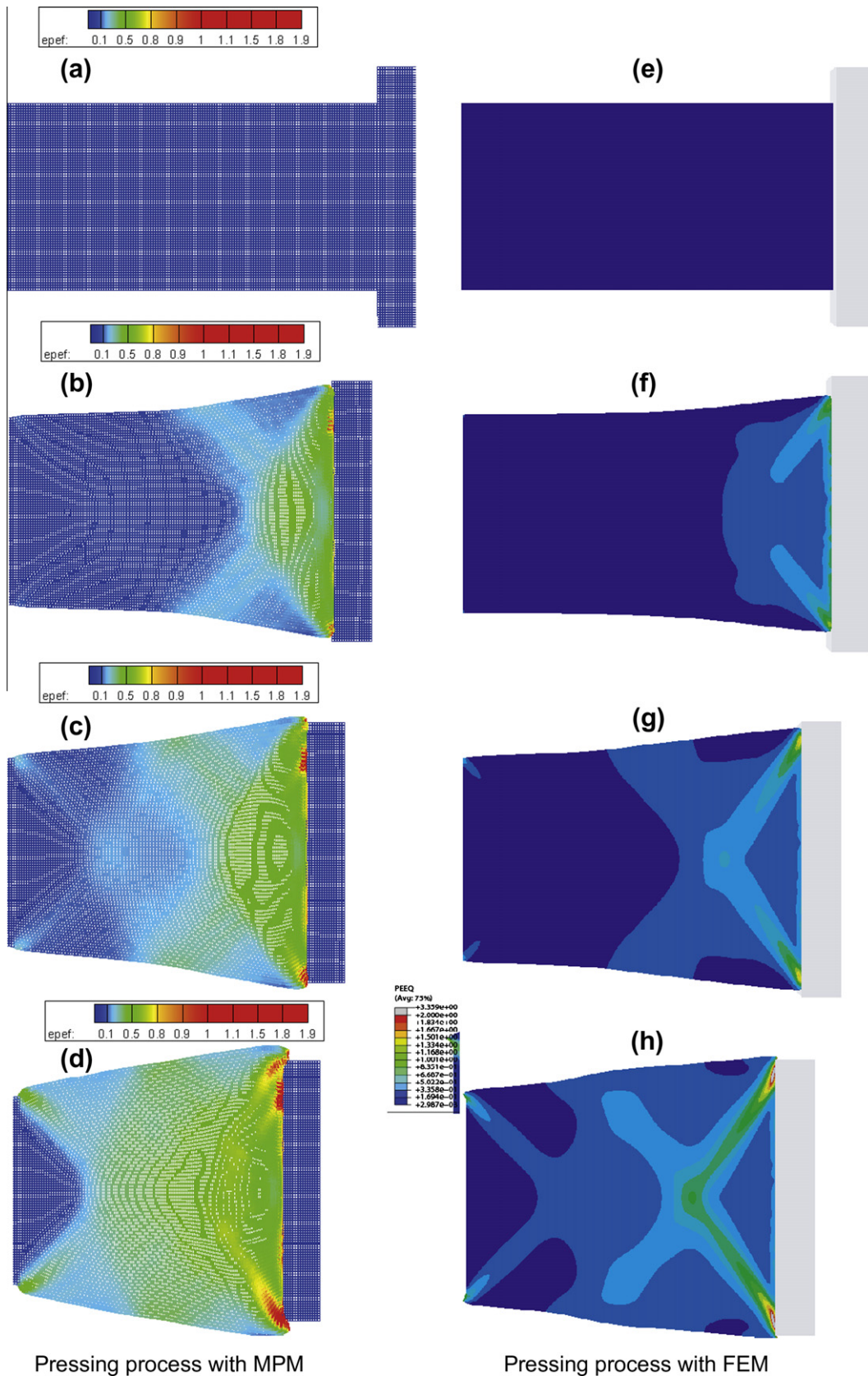
Table 2
Johnson–Cook parameter values for AISI 4340.

A (initial yield stress in MPa)	792
B (hardening modulus in MPa)	510
n (work hardening exponent)	0.26
C (strain rate dependency coefficient MPa)	0.014
m (thermal softening coefficient)	1.03

3. Computational simulations

Initially the numerical set-up for the cutting process computations with FEM as well as with MPM is described. The similar numerical modeling has been carried out for FEM and well as for MPM. The model set-up is shown in Fig. 2.

Horizontal and vertical displacements are constrained for bottom and left side nodes of the workpiece. Constant velocity has been applied for the tool. Also there is a possibility to apply boundary velocity to the work-piece, but it incurs complexities to define the chip flow direction. The tool is modeled with rigid material, as the concerned importance is given to the work-piece analysis during cutting process. The workpiece in present contribution is assumed under plane strain condition.

The MPM introduced in the previous sections is implemented in a C++ programm and verified for different applications [21–23]. In the present paper the MPM will be further compared with the FEM in pressing and cutting process simulations. During MPM computations the importance of contact with consideration of friction is explained. The FEM computations are performed using the general purpose commercial finite element code ABAQUS [29]. For transient processes of AISI4340 steel modeled with Johnson–Cook material model is used to describe the material property [27,28],

$$\sigma_e = [A + B(\varepsilon^p)^n]\left[1 + C\ln\left(\frac{\dot{\varepsilon}^p}{\dot{\varepsilon}^0}\right)\right],$$

$$\left[1 - \left(\frac{T - T_{\text{room}}}{T_{\text{melt}} - T_{\text{room}}}\right)^m\right], \tag{24}$$

where σ_e denotes the effective flow stress, ε^p the equivalent plastic strain, $(\dot{\varepsilon}^p/\dot{\varepsilon}_0)$ stands for non-dimensional plastic strain rate. T_{Room} is the room temperature, T_{Melt} is the melting temperature of the material. A, the initial yield stress (MPa); B, the hardening modulus; n, the work hardening exponent; C, the strain rate dependency coefficient (MPa); and m is the thermal softening exponent. The material parameters are summarized in Table 1. The Johnson–Cook model is popular in cutting process simulations. For AISI 4340 material the Johnson–Cook constitutive equation parameters are given in Table 2.

In an adiabatic process heat conductance is neglected and the fraction of mechanical work converted into heat only at the integration points. This fraction is defined with Taylor–Quinney factor, η, as

$$\rho C_p dT = \eta \boldsymbol{\sigma} \cdot \boldsymbol{\varepsilon}^p, \tag{25}$$

where ρ denotes material density, C_p specific heat, dT temperature change. Here the Einstein's summation convention is used. From the above formulation it is easy to calculate temperature values at the integration points, if the stresses and strains are known, whereas in thermo-mechanical coupling process temperature is calculated based on heat conduction equation which should be solved with the equilibrium equations simultaneously.

3.1. Pressing process simulations

The material block is of AISI4340 steel modeled with Johnson–Cook material model and the press is modeled with rigid

Fig. 3. Schematic representations of plastic strain distribution for pressing process simulations with MPM and FEM.

model. The left side nodes of the block are fixed, and right end left for free. The geometrical sizes of the block and the press are 1 mm × 0.5 mm × 0.1 mm and 0.1 mm × 0.7 mm × 0.1 mm, respectively. A constant velocity of 200 m/s is applied to the press. The number of particles used for the block are 183,616 and 27,136 for the press. Same number of nodes are applied for FEM mesh for
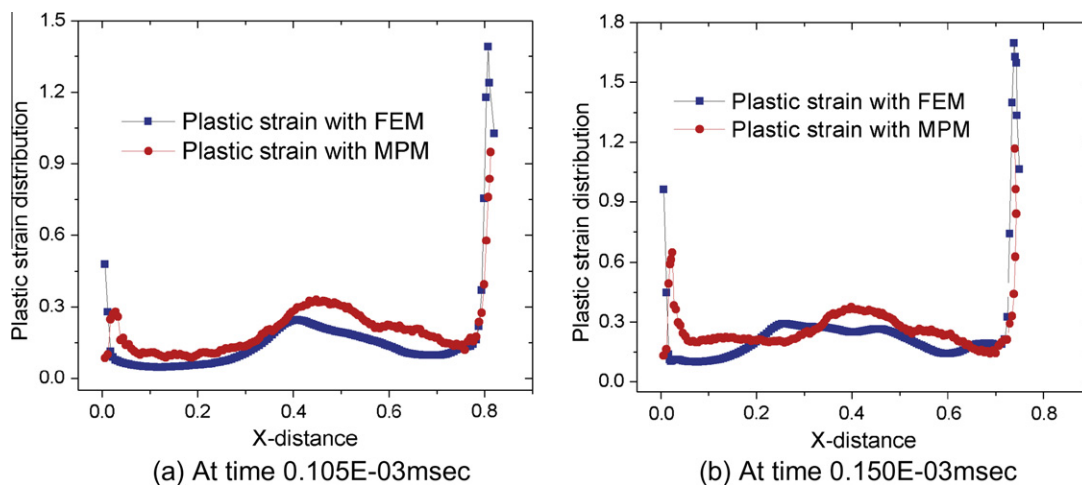
(a) At time 0.105E-03msec

(b) At time 0.150E-03msec

Fig. 4. Comparison of plastic strain distribution with *x*-distance in MPM and in FEM.

Table 3
Information about computational model.

Type of material used	AISI4340 steel
Material model for workpiece	Johnson–Cook
Material model for tool	Rigid
Velocity for the tool	50 mm/ms
Feed	0.3 mm and 0.5 mm
Workpiece size	3 mm × 1 mm
Tool size	0.5 mm × 1 mm
Number of particles for workpiece	120,000
Number of particles for tool	20,000

the pressing process simulation. With the given description the numerical simulations are performed with MPM and FEM methods. Here only equivalent plastic strain distribution is compared between two methods.

Fig. 3a–d present results of the pressing process simulations with MPM and Fig. 3e–h represents the pressing process simulations with FEM. Here equivalent plastic strain distribution is compared between MPM and FEM. The maximum value of plastic strain is limited to two in both cases for better viewing of strain distribution. The plastic strain distribution in both cases is approximately similar. The localization of strains from MPM is not clearly observed, this is mainly caused by the number of material points. With increasing number of material points, strain localization can be seen more effectively. For better comparison of plastic strain distribution between MPM and FEM computations, plots are drawn between x-distance value and plastic strain distribution (Fig. 4). The plastic strain distribution shown in Fig. 4a corresponds to Fig. 3c and g, and Fig. 4b corresponds to Fig. 3d and h, respectively. Here we can observe similar distribution of plastic strain. From Fig. 4b, the strain distribution at the left side of the block increases with increasing the press displacement. Slight changes in the strain distribution comes from the different methods applied. Generally one would expect lower accuracy in the MPM.

3.2. Cutting process simulations using GIMPM and FEM

The present MPM code is developed with C++ programming language. For MPM computations 120,000 particles are used for the work-piece with size 3 mm × 1 mm. Total computation time with MPM is 37027.8 s. For computations HP Z400 work station with INTEL XEON CPU was used. This is 4 processor CPU with 6 GB RAM.

In cutting process the shear band and strain localization play an important role. Due to localized high strains, the FEM elements are distorted significantly and simulation results are sensitive to the element size [7,8]. The accuracy of the numerical computations drops with element distortion. In an implicit computation the FEM fails to converge. As MPM does not contain any finite element mesh, this method is advantageous over FEM. It contains only background mesh on which the field variables are updated using material points. The material points carry all the information needed and the cell is fixed in the space.

Detailed information about the computational model is given in Table 3. The computations are run under plane strain condition, some assumptions are made to simplify the model. The tool is assumed as rigid. Some research works demonstrated importance of the deformable tools [15], especially for analysis of wear damage of tool. For present simulations tool wear will not considered. The cutting velocity is very high to reduce computation time. Such simplifications will not affected the simulation qualitatively.

The main influencing parameters in GIMPM are the distance between the two nodes, distance between the particles and contact phenomenon applied. Generally we assign the distance between two nodes (cell distance) is approximately two times of the distance between two particles. Some times negative volume occurs in the particles during computation, it is mainly due to high strain values at the particles or at cell nodes. This can be remedied by reducing velocity of the tool. Fig. 5 plots plastic strain and temperature distributions from both MPM and FEM computations. In Fig. 5a and b the plastic strain distribution is similar between both methods. The comparison is done based on plastic strain and temperature because these are the two main parameters which influence the cutting process significantly. One may observe essentially a similar chip morphology from both computations which implies that both methods generate averagely the same deformations. In local regions, the differences can be found in both strain and temperature distributions. The MPM predicts generally smoother results in both plastic strain and temperature distribution due to its rougher interpolation algorithm. High strain rates can be easily handled by the MPM, as particles store all the necessary information at the state of the calculation. Hence no numerical errors occur due to mesh returning to its original state. But numerical errors may occur due in updating field variables on material points by mapping the nodal values with shape functions. Later again this material points data will be mapped to grid nodes. This transformation of data between material points and background mesh may admit slight changes. This method uses Lagrangian solid particles embedded in an Eulerian grid.

Fig. 6a represents the plastic strain value at each material point when the tool moves a distance of 2 mm from right side with
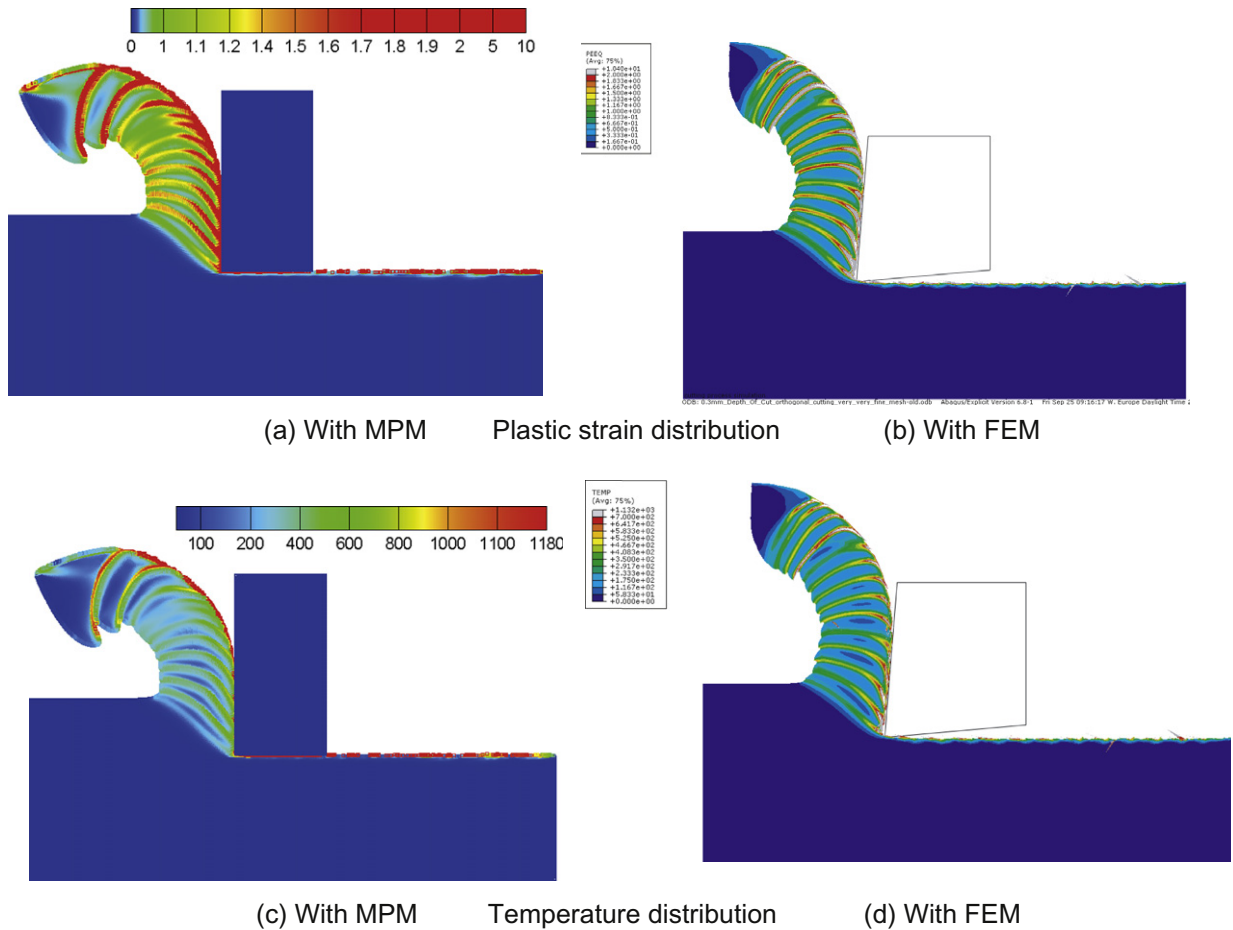
Fig. 5. Comparison of plastic strain and temperature distribution between MPM and FEM simulations. (a) Plastic strain from MPM. (b) Plastic strain from FEM. (c) Temperature from MPM. (d) Temperature from FEM.
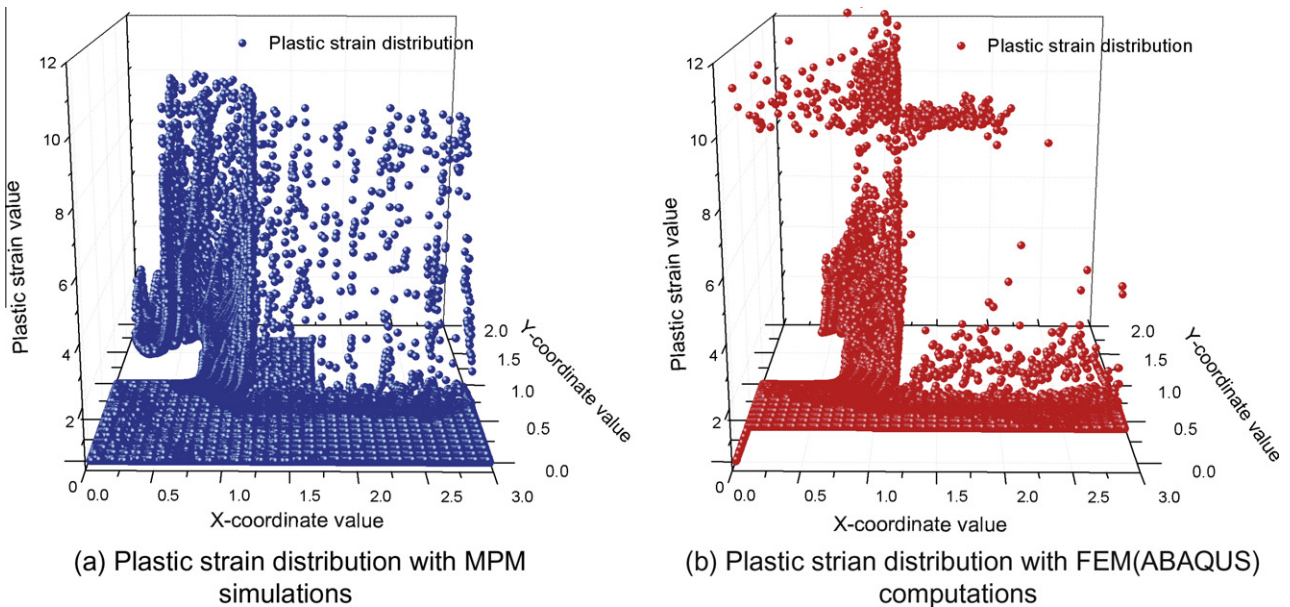

Fig. 6. Schematic representation of the plastic strain distribution of the whole workpiece. The x coordinate denotes the length direction of the workpiece, y stands for the height direction. (a) MPM results. (b) FEM (ABAQUS) results.

GIMPM method. Particle identification is done by x and y coordinate values. Here x is the cutting direction, y denotes the height of the workpiece. Similarly, Fig. 6b represents the plastic strain values at the integration points for FEM computations. Fig. 6a and b
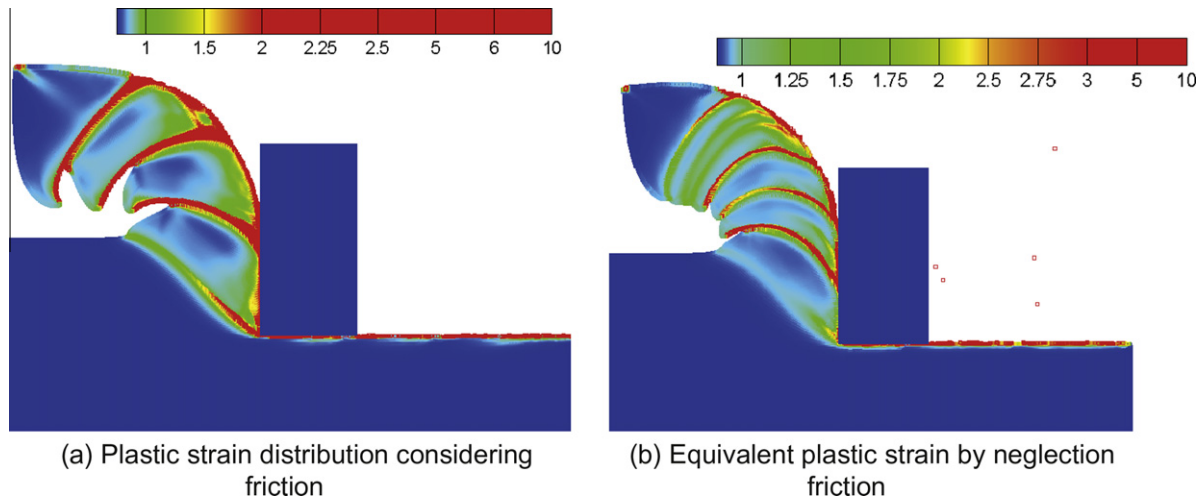
(a) Plastic strain distribution considering friction

(b) Equivalent plastic strain by neglection friction

Fig. 7. Effects of friction on the shear band formation. (a) With friction. (b) No friction.

(a) Temperature distribution with 0.5mm feed

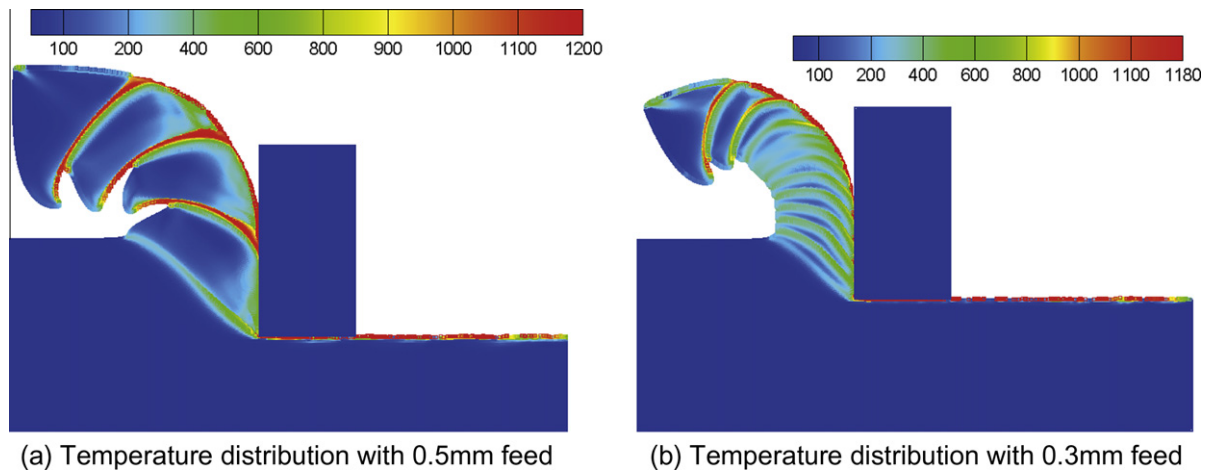(b) Temperature distribution with 0.3mm feed

Fig. 8. Influence of feed on chip morphology and shear band formation. (a) With 0.5 mm feed. (b) With 0.3 mm feed.

are related to Fig. 5a and b, respectively. Fig. 6 is informative to describe the chip morphology effect, stability region, residual stress and strains, etc. The region between $x = 0.55$ mm and 1.05 mm in Fig. 6 is represented by effective shear banding region from Fig. 5. Thus one can observe high plastic strains in the range of $x = 0.55$–1.05 mm. When the instability condition is defined with maximum plastic strain value, the stability region is identified very easily with Fig. 6. The region above the maximum plastic strain defined for material failure is treated as instability region. The chip morphology is explained as the distribution of plastic strain below $x = 0.55$ mm. The distribution of plastic strain with MPM (Fig. 6a) below $x = 0.55$ mm is more, that identifies the bending of chip is more with MPM. Chip morphology is not absolutely similar in both the computations (MPM and FEM). Residual strain is more with MPM calculation, this observation is concluded from Fig. 6a. Heavy strain distribution traces are identified on the machined surface of workpiece. Where as with FEM (Fig. 6b) the residual strains are minimal on machined surface.

FEM contains the mesh, as the cutting process progresses element distortion increases which leads to decrease in time step. The time step keep on decreases with increasing mesh distortion. When the time step reduces to certain level the computation will be terminated. This problem has been overcome with GIMPM computations as there is no mesh present to distort. With GIMPM

simulations after each step the background grid returns to its original position. No numerical errors occurs due mesh returning to its original position as all the information is carried out by the particles. Where as FEM incurs errors as the mesh returning to its original position while computation. In MPM nodes remain fixed on a regular grid, hence computation of gradients is trivial. All these advantages of GIMPM enhances the applicability of this method for high deformation processes. The smoother simulations with MPM method have been seen.

3.3. Effect of friction on shear band formation

Friction has significant effects on the formation of shear bands. With the absence of friction mild shear bands and with consideration of friction intense shear bands can be observed, which are confirmed in Fig. 7. The effect of contact considering friction leads to intensified formation of shear bands. The coefficient of friction used in the present contribution is $\mu = 0.2$. There is no lubricant used for the process simulations, hence the contact friction between tool and workpiece is treated as dry friction. Friction generates additional heat to the chip formation. When there is no friction between two bodies, the tool moves on the workpiece without any resistive force. Thus the amount of energy dissipation is less. The formation of shear bands in cutting is due to mechanical

work converted into heat. When the mechanical work is less, the amount of heat produced is also less. Therefore less intense shear bands can be observed in the absence of friction.

3.4. Influence of feed on shear band formation

The shear instability occurs when the heating due to plastic energy dissipation is large enough. Due to this heating the material softens, material hardens as it deforms. This tendency leads to formation of shear bands. Here with increasing feed (depth of cut) the cutting force increases, thus the energy dissipation increases. The produced mechanical energy is converted into heat and tends to soften the material which leads to formation of shear bands in the localized area of primary shear zone (Fig. 8). With increasing feed the width of shear band reduces, this is mainly due to increase in localization leads to contraction of shear band and increase in teeth size. The frequency of shear band formation decreases with increasing feed (Fig. 8). With increasing feed the distance between two instability effects increases, because of increasing in chip thickness.

4. Conclusions

Detailed discussion about the MPM and GIMPM methods for cutting process simulation has been summarized in the present work. The advantages and disadvantages of MPM method are phrased. To verify the adaptability of MPM for high deformation processes, initially pressing process is simulated and the plastic strain distribution is compared with FEM simulation results. The comparison confirms that the MPM generates essentially the same results as the FEM (see Figs. 3 and 5).

GIMPM is developed for cutting process simulation. The plastic strain and temperature distributions of GIMPM are compared with FEM results. It is found that the GIMPM provides a smoother numerical results which leads to less strain localizations in the chip formations. The trend of the shear band formation and temperature distribution in both cases is similar. Spatial distribution of plastic strain values with respect to X and Y coordinate values gives the scope to analyze chip morphology, residual strain values on machined surface and stability region.

The effect of friction on process simulations is discussed with GIMPM. Strong localization can be observed by considering friction. In the absence of friction the intensity of shear band formation is not effective. Further the influence of feed on shear localization has been explained. With increasing feed the localization phenomenon increases, thus leads to contraction of shear bands and formation of teeth.

The improvements have to be done in the area of contact criterion applied considering friction phenomenon to derive sticking force, sliding force, tangential force, etc. Material failure has major scope in machining simulations, hence it is required to improve

algorithm to define material failure with the available techniques (maximum stress, maximum strain, plastic displacement criterion, etc.). Further investigation on influencing parameters of MPM can be done.

References

[1] M. Eugene Merchant, Journal of Applied Physics 16 (1945) 318–324.
[2] M. Eugene Merchant, Journal of Applied Physics 16 (1945) 267–275.
[3] J.S. Strenkowski, J.T. Carroll, Journal of Engineering for Industry 107 (1985) 349–354.
[4] J.T. Carroll, A numerical and experimental study of single point diamond machining, Ph.D. Thesis, North Carolina State University, 1987.
[5] D.H. Howerton, An experimental and numerical investigation of orthogonal machining of aluminum 6061-T6, Ph.D. Thesis, North Carolina State University, 1989.
[6] J.D. Oh, J.C. Aurich, A finite-element-analysis of orthogonal metal cutting processes, in: Proceedings 8th International Conference on Numerical Methods in Industrial Forming Processes, 2004, pp. 1390–1395.
[7] R. Ambati, H. Yuan, International Journal of Advanced Manufacturing Technology (2010).
[8] R. Ambati, H. Yuan, Application of linear perturbation analysis for cutting process simulations, submitted for publication.
[9] T. Özel, E. Zeren, International Journal of Advanced Manufacturing Technology 35 (2007) 255–267.
[10] M. Movahhedy, M.S. Gadala, Y. Altinas, Journal of Materials Processing Technology 103 (2000) 267–275.
[11] O. Pantalé, R. Rakotomalala, M. Touratier, International Journal of Forming Processes 1 (3) (1998) 371–388.
[12] M. Heinstein, D. Segalman, Simulation of Orthogonal Cutting with Smooth Particle Hydrodynamics, Sandia National Laboratories, 1997.
[13] J. Limido, C. Espinosa, M. Salaün, J.L. Lacome, International Journal of Mechanical Sciences 49 (2007) 898–908.
[14] F.H. Harlow, Methods in Computational Physics 3 (1964) 319–343.
[15] J. Monaghan, T. MacGinley, Computational Materials Science 16 (1999) 275–284.
[16] D. Sulsky, Z. Chen, H.L. Schreyer, Computer Methods in Applied Mechanics and Engineering 118 (1994) 179–196.
[17] S.G. Bardenhagen, J.U. Brackbill, D. Sulsky, Computer Methods in Applied Mechanics and Engineering 187 (2000) 529–541.
[18] S. Bardenhagen, E. Kober, Computer Modeling in Engineering and Sciences 5 (2004) 477–495.
[19] S. Bardenhagen, Journal of Computational Physics 180 (2002) 383–403.
[20] S. Bardenhagen, J. Guilkey, K. Roessig, J. Brackbill, W. Witzel, J. Foster, Computer Modeling in Engineering and Sciences 2 (2001) 509–522.
[21] X. Zhang, K.Y. Sze, S. Ma, International Journal for Numerical Methods in Engineering 66 (4) (2006) 698–706.
[22] X.F. Pan, A. Xu, G. Zhang, J. Zhu, Journal of Physics D: Applied Physics 41 (2008) 9.
[23] X.F. Pan, A. Xu, G. Zhang, P. Zhang, J. Zhu, S. Ma, X. Zhang, Communications in Theoretical Physics 49 (5) (2008) 1129–1138.
[24] L. Moresi, F. Dufour, H.B. Mühlhaus, Journal of Computational Physics 184 (2003) 476–497.
[25] M. Bäker, Computational Materials Science 33 (2004) 407–418.
[26] M. Bäker, Computational Materials Science 26 (2003) 175–182.
[27] G.R. Johnson, W.H. Cook, A constitutive model and data for metals subjected to large strains, high strain rates and high temperatures, in: Proceedings of the Seventh International Symposium on Ballistics, 1983, pp. 541–547.
[28] G.R. Johnson, W.H. Cook, Engineering Fracture Mechanics 21 (1) (1985) 31–48.
[29] ABAQUS User's Manual, Version 6.9, Simulia Inc., Providence, RI, 2009.
[30] T. Özel, E. Zeren, Finite element modeling the influence of edge roundness on the stress and temperature fields induced by high-speed machining, International Journal of Advanced Manufacturing Technology 35 (2007) 255–267.